Selçuk Üniversitesi Fen Fakültesi Fen Dergisi 48 (1) 2022 Sayfa 34-45

Mevcut sayıya ait içindekiler listesine DergiPark üzerinden ulaşılabilir

Selçuk Üniversitesi Fen Fakültesi Fen Dergisi

Dergi web sayfası: dergipark.org.tr/tr/pub/sufefd

Research Article

Phase modulation of MoO_2 -MoO_3 nanostructured thin films through W-Doping; utilizing UV photodetection and gas sensing applications

Shrouk. E. Zaki [a,1,3], Mustafa Buyukharman [b,1,2], Mohamed A. Basyooni [c,1,3], Arife Efe Görmez [d,4], Ayşegül Sezgin [e,1], Yasin Ramazan Eker [f,5], Mücahit Yılmaz [g,1,*]

[1] *Department of Nanoscience and Nanoengineering, Institute of Science and Technology, Necmettin Erbakan University, Konya, 42090, Turkey*
[2] *Department of Physics, Faculty of Science, Istanbul University, Istanbul 34134, Turkey*
[3] *Department of Nanotechnology and Advanced Materials, Graduate School of Applied and Natural Science, Selçuk University, Konya 42030, Turkey*
[4] *Department of Nanoscience and Nanoengineering, Institute of Science and Technology, Ataturk University, Erzurum 25240, Turkey*
[5] *Department of Metallurgy and Material Engineering, Faculty of Engineering and Architecture, Necmettin Erbakan University, Konya 42060, Turkey*

ARTICLE INFO

Article History
Received 19 February 2022
Revised 15 April 2022
Accepted 16 April 2022

Keywords
Photodetector
Gas sensor
Thin-film
Metal oxide
Semiconductor
Nanostructure

ABSTRACT

Gas sensing properties of metal oxide semiconductors draw high attention due to their simple fabricating methods, and low cost, chemical, and physical properties. In general, a high bandgap (>2 eV) can cause them to react in the UV region through the electromagnetic spectrum. Controlling the UV-photodetection and gas sensing ability of MoO_2-MoO_3 thin film through tungsten (W) doping of different ratios have been reported here. The preparation of these films was grown using a reactive magnetron sputtering system with different power sputtering of W-content. The bandgap calculations showed that the samples have a wide bandgap value. A small particle size of 8nm was observed through high W doping concentration which enhanced these materials toward high efficient gas sensing and UV photodetector applications. The UV optical sensor exhibits a high responsivity value of 2500A/W and an external quantum efficiency (EQE) value of 5x109 at 365nm. Also, an increase in the photocurrent gain value with increasing the W amount with a maximum value of 0.13, while a photocurrent of 1mA was observed. On the other hand, a fast-response/recovery time-based CO2 gas sensor of less than 10 sec was observed. The thin-film sensors showed well-defined adsorption and desorption kinetics in a CO_2 environment with a p-type chemisorption behavior.

Araştırma Makalesi

MoO_2-MoO_3 nanoyapılı ince filmlerin W-Doping yoluyla faz modülasyonu; UV foto ve gaz algılama uygulamalarını kullanma

MAKALE BİLGİSİ

Makale Geçmişi
Geliş 19 Şubat 2022
Revizyon 15 Nisan 2022
Kabul 16 Nisan 2022

Anahtar Kelimeler
Fotodedektör
Gaz sensörü
İnce tabaka
Metal oksit
Yarı iletken
Nanoyapı

ÖZ

Metal oksit yarı iletkenlerin gaz algılama özellikleri, basit üretim yöntemleri ve düşük maliyeti, kimyasal ve fiziksel özellikleri nedeniyle büyük ilgi görmektedir. Genel olarak, yüksek bir bant aralığı (>2 eV), elektromanyetik spektrum yoluyla UV bölgesinde reaksiyona girmelerine neden olabilir. Farklı oranlarda tungsten (W) dopingi yoluyla MoO_2-MoO_3 ince filmin UV foto algılama ve gaz algılama yeteneğinin kontrol edilmesi burada rapor edilmiştir. Bu filmlerin hazırlanması, W içeriğinin farklı güç püskürtmeli reaktif magnetron püskürtme sistemi kullanılarak büyütüldü. Bant aralığı hesaplamaları, örneklerin geniş bir bant aralığı değerine sahip olduğunu göstermiştir. Bu malzemeleri yüksek verimli gaz algılama ve UV fotodetektör uygulamalarına doğru geliştiren yüksek W katkı konsantrasyonu yoluyla 8 nm'lik küçük bir parçacık boyutu gözlemlendi. UV optik sensör, 365nm'de 2500A/W'lik yüksek bir duyarlılık değeri ve 5x109'luk bir harici kuantum verimliliği (EQE) değeri sergiler. Ayrıca, 1mA'lık bir fotoakım olurken, maksimum 0.13 değerinde W miktarı arttıkça fotoakım kazanç değerinde bir artış gözlemlendi. Öte yandan, 10 saniyeden kısa bir hızlı yanıt/kurtarma süresine dayalı CO2 gaz sensörü gözlendi. İnce film sensörleri, p-tipi kimyasal adsorpsiyon davranışına sahip bir CO_2 ortamında iyi tanımlanmış adsorpsiyon ve desorpsiyon kinetiği gösterdi.

* Sorumlu Yazar
E-posta adresleri: mucahityilmaz@erbakan.edu.tr (M. Yılmaz), shrouk.e.zaki@gmail.com (S. E. Zaki), mbykharman@gmail.com (M. Buyukharman), m.a.basyooni@gmail.com, (M. A. Basyooni), arifefe_90@hotmail.com (A. E. Görmez), aysegul14761@gmail.com (A. Sezgin), yeker@erbakan.edu.tr (Y. Eker)
[a] ORCID: 0000-0002-5097-1070, [b] ORCID: 0000-0002-9111-0904, [c] ORCID: 0000-0001-8473-8253, [d] ORCID: 0000-0001-6134-7487, [e] ORCID: 0000-0003-3933-4748, [f] ORCID: 0000-0001-7395-4364, [g] ORCID: 0000-0002-3387-5095

Doi: 10.35238/sufefd.1068674
E-ISSN: 2458-9411

1. Introduction

Metal oxide semiconductors (MOSs) sensors, a type of thin-film sensor that changes resistance depending on the chemical environment (chemo-resistive sensor), have recently achieved high sensitivity levels, indicating that they could be used for both indoor and outdoor gas detection applications (M. A. Basyooni, Zaki, et al., 2020). Owing to the reliable sensitivity, low cost, low production, simplicity, and the gas detectivity, the MOSs nanostructures such as WO_3 (Jung et al., 2020; Zeb et al., 2019), MoO_3 (M. A. Basyooni, Zaki, et al., 2020), ZnO (Akdağ et al., 2016), Nb_2O_3 (Boström et al., 2004), SnO_2 (Haider et al., 2013; Shaban et al., 2014, 2015), Fe_2O_3 (Bashiri et al., 2020) and In_2O_3(Ma et al., 2019) are widely implemented. Among them, MoO_3 and WO_3 are reported to have promising electrical and optical properties for various applications such as solar cells, gas sensing (Z. Wei et al., 2018) smart windows application (Bin Li et al., 2019), display devices (Yeh et al., 2018), energy storage devices (Xu et al., 2019), electrodes (Yue et al., 2020), perovskite solar cells (B. S. Kim et al., 2015) and transistors (Sun et al., 2010), and also it is very common to use as sensing layer (Mohamed et al., 2019).

CO_2 has recently emerged as the most significant greenhouse gas contributing to global warming and climate change. The detection of CO_2, which is a blackdamp, is also critical. Because of their advantages for CO_2 detection, MOS-based detection devices are one of the most promising gas sensors (Juang & Chen, 2020). Studies for sensitive and fast-response gas sensors for the detection of toxic and greenhouse gases received high attention. Also, CO_2 gas detection is important in different applications such as fire/air detection, food quality control, industrial processes, and medical diagnostics (Juang & Chen, 2020). Researchers reported on several CO2 gas sensors that are MOS-based such as ZnO (Çolak & Karaköse, 2019; Ghosh et al., 2019), CuO (N. Bin Tanvir et al., 2015; N. B. Tanvir et al., 2017), and SnO_2(Hsu et al., 2020). Gas sensors and photodetectors based on MOSs are widely studied by many authors. Among many transition metal oxides, Molybdenum oxide (MoO_3) is a wide bandgap semiconductor that implements high permission for gas sensor optoelectronic devices due to its controllable production, low cost, and fast response (Jiang et al., 2019). For instance, in previous studies, MoO_3 is sensitive to different gases such as SO_2, H_2S (Çiftyürek et al., 2016), ethanol (T. Li et al., 2015; Mo et al., 2020; Touihri et al., 2017), H_2 (Shafieyan et al., 2019; S. Yang et al., 2019), and triethylamine (He et al., 2019; Q. Wei et al., 2019), NO_2 (Mane & Moholkar, 2018), H_2O_2(Bo Li et al., 2019), and CO_2 (M. A. Basyooni, Zaki, et al., 2020).

On the other hand, MoO_3 is important in photoelectric devices and their applications because of its optoelectronic and electrical properties. J. Kim *et al.,* studied the photodetector behavior of MoO_3/Si heterojunction under the infrared (IR) illumination with a fast response of 72.32ms and recovery time of 68.15ms. (Park et al., 2018). While, in a study by Q. Zheng *et al*., the MoO_3-based flexible ultraviolet photodetector has been implemented with a high on/off switching ratio over two orders, a response time of less than 1sec, and high responsivity of 183 mAW^{-1} (Zheng et al., 2015). Moreover, many studies have been reported before (Lee et al., 2019; Pal et al., 2020; Zhao et al., 2015). The addition of specific extrinsic elements to MOS will affect many properties such as surface activity, electron mobility, defect and grain size,... etc. Among these additives, the W element draws great attention. Results of a study conducted by G. Lu *et al.,* showed a gas sensing performance of W doping NiO is approximately 139 times higher than pristine NiO (Wang et al., 2015). P. Song *et al.,* reported high trimethylamine sensing performances towards W doped MoO_3 developed (Z. Li et al., 2017).

We used W doping to investigate the effect of MoO2 and MoO3 ratios. Controlling the O2 concentrations during the sputtering process was used to accomplish this. The major goal of this work was to understand the main role of the crucial amount of O2 and Mo through the deposited thin films utilizing XRD - Rietveld refinement analysis using the Fullproof tool. This work shows structural, morphology, topography, and optical characterizations of Mo-O through different concentrations of 0, 20, and 40% of W-doped. By focusing on the behavior of W on MoO_2 - MoO_3 lattice, gas sensing applications, the direct optoelectronic behavior, bandgap calculations, and UV photodetector have been examined.

2. Materials and Methods

2.1. Preparation of W doped Mo-O thin film

W-doped MoO_2-MoO_3 composite nanostructured thin films of 0, 20, and 40 % that denoted by W_0, W_2, and W_4, respectively. The deposition process was conducted by using a magnetron sputtering system (3M1T VAKSİS MİDAS) based on 99.9% high purity Mo and W targets. Carrier gas of Argon (Ar) and reactive gas of Oxygen (O_2) are used to control the deposition of the oxide thin films. Under a vacuum condition of $3x10^{-7}$ Torr, the sputtering temperature of 400° C, sputtering time of 90 min, the working pressure of $5x10^{-3}$ Torr, and different W power intensity, the W-doped MoO_3-MoO_2 formed. A gas flow meter was used to control the flow of O_2 and Ar gas. Fused silica and FTO on glass substrates are cleaned for 15 minutes in acetone and IPA in the ultrasonic bath, then rinsed with DI water and dried with N_2 gas.

2.2 Characterization techniques

The structural and crystal characterizations were done by the APD2000 X-ray diffractometer, using λ = 1.54 Å (CuK_α) in the scanning range of 10-90° with 0.01° step. The recorded XRD data are analyzed using Fullproof Suite software based on the Rietveld structure refinements program of MoO_3 thin films [45]. Then, the calculated structure was visualized in a 3D view using VESTA software. Renishaw inVia confocal Raman spectroscopy system and TESCANMAIA3 XMU model were used for Raman and scanning electron microscopy (SEM) measurements, respectively. Raman measurements were conducted with a 532 nm laser beam. Quantitative analysis of the elements was carried out with Oxford 50Xmax by energy-dispersive X-ray (EDX) analysis. The surface topography and thickness of films were taken using Park XE6 Atomic Force Microscopy (AFM). The transmission (T) and absorption (A) spectrums were taken using Shimadzu UV-VIS Spectrophotometer. The bandgap (E_g) of the deposited thin films was calculated using the Tauc equation. The electrical, optoelectronic, and gas sensing measurements were measured based on Keithley SourceMeter with the help of a UV light source that emits 365 nm. Our previous studies show the details of the gas sensing measurement system (M. A. Basyooni, Eker, et al., 2020; M. A. Basyooni, Zaki, et al., 2020; M. A. M. A. Basyooni et al., 2017; Görmez et al., 2020; Zaki et al., 2019).

3. Results and Discussions

3.1. Structural properties

The XRD patterns of W_0, W_2, and W_4 samples are shown in Fig. 1, 2, and 3. As shown in Fig. 1 and 2, a low concentration of W content contributes to the high crystallinity of the MoO_2-MoO_3. However, the amorphous peak in Fig. 3 for W_4 thin film could be due to a higher concentration of W. This phenomenon may get raised by the fact that the enthalpy of Mo-O (560.2 ± 20.9 kJ/mol) is lower than that of the enthalpy of W-O (672.0 ± 41.8 kJ / mol), which means that Mo requires less energy to form a compound with oxygen ("CRC Handbook of Chemistry and Physics. 81st Edition Edited by David R. Lide (National Institute of Standards and Technology). CRC Press: Boca Raton, FL. 2000. 2556 Pp. $129.95. ISBN 0-8493-0481-4," 2000). Due to the importance of oxygen vacancy calculations and refinement analysis in transition metal oxides, the XRD Rietveld refinement structure of W_0, W_2, and W_4 thin films are calculated and plotted as in Fig. 1, 2, and 3. For the W_0 thin film, the R-factors; R_{wp}, $R_{exp,}$ and χ^2 are equal to 7.52, 3.26, and 5.31, respectively. The distribution of the unit cell and atoms of W_0 are plotted and depicted in Fig. 1 (b) and summarized in Table 1.

Table 1
Unit cell parameters of W_0, W_2, and W_4 thin films.

Sample	Phase	a (Å)	b (Å)	c (Å)	α (°)	β (°)	γ (°)
W_0	*WO_3*	-	-	-	-	-	-
	MoO_2	9.788	8.604	4.714	90.00	90.00	90.00
	MoO_3	15.309	3.719	3.976	90.00	90.00	90.00
W_2	*WO_3*	18.272	3.818	14.070	90.00	115.02	90.00
	MoO_2	9.828	8.639	4.677	90.00	90.00	90.00
	MoO_3	15.249	3.716	3.978	90.00	90.00	90.00
W_4	*WO_3*	18.508	3.759	14.033	90.00	115.21	90.00
	MoO_2	9.198	8.591	4.809	90.00	90.00	90.00
	MoO_3	14.884	3.778	4.035	90.00	90.00	90.00

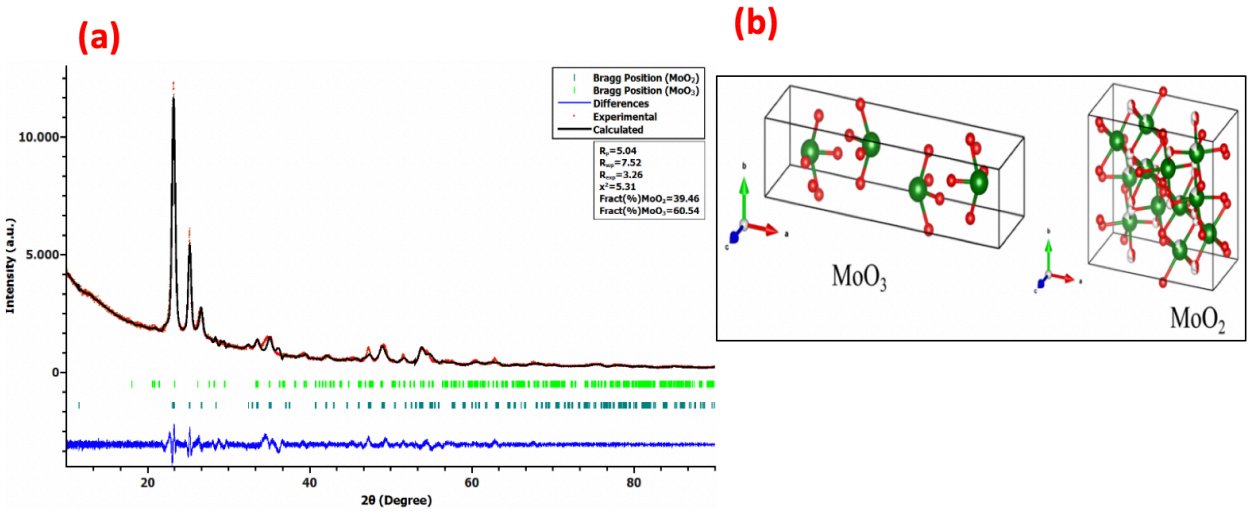

Figure 1. (a) and (b) show the XRD Rietveld structure refinement pattern and the unit cells of W_0-doped MoO_3 thin film, respectively.

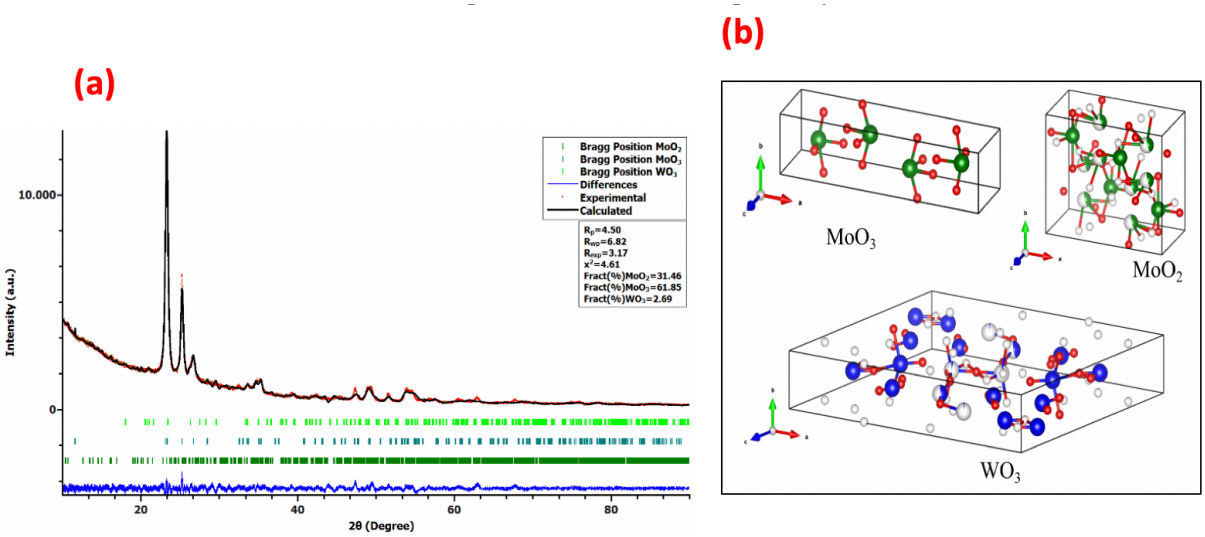

Figure 2. (a) and (b) show the XRD Rietveld structure refinement pattern and the unit cells of W_2-doped Mo-O thin film, respectively.

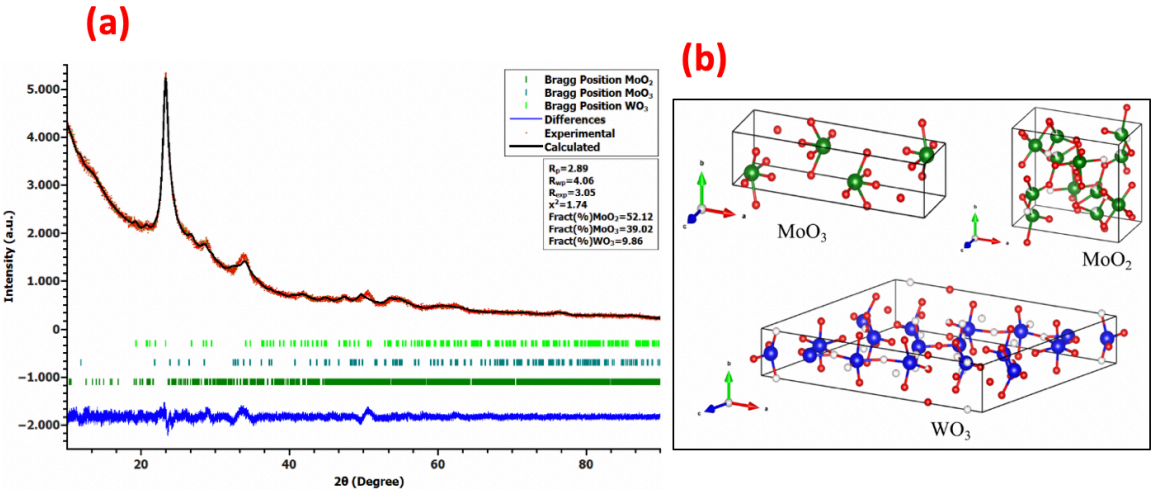

Figure 3. (a) and (b) show the XRD Rietveld structure refinement pattern and the unit cells of W_4-doped Mo-O thin film, respectively.

Table 2 also shows the W_0 sample's lattice characteristics, Mo-O_2 content, and phase percentages. The Rietveld structure refinements produced from XRD data and unit cells of the thin film structure are shown in Figures 1, 2, and 3. In the MoO_2 phase, W_0 had a crystal structure of 39.46 %, and in the MoO_3 phase, it had a crystal structure of 60.54%. R-factors of refined structures of samples show a decrease with an increase in the W doping concentration as shown in Fig. 1(a), 2(a), and 3(a). Both R factors and χ^2 values show that the refinement processes of samples are within acceptable limits. The percentage of MoO_2, MoO_3, and WO_3 structures are calculated based on XRD Rietveld refinement and indicated in Table 2 as 31.46%, 61.85%, and 2.69%, respectively. With the increase in W doping amount, an increase in the amount of MoO_2 in the structure was observed. The W-O compound formed in the structure is not exactly WO_3, but it is more suitable for the $WO_{2.72}$ structure which is one of the sub-oxides of the W-O system. The unit cells of the Mo-O and W-O structures drawn from the VESTA program and whose parameters are derived from the Rietveld analysis are shown in Fig. 1(b), 2(b), and 3(b). Unit cell parameters for MoO_2, MoO_3, and WO_3 structure are indicated in Table 1, amount and phase percentage of W, Mo, and O_2 are shown in Table 2.

Table 2
Shows the XRD Rietveld refinement structure analysis of W_0, W_2, and W_4 thin films.

Sample	Phase	Amount of W	Amount of Mo	Amount of O_2	Ratio of O/W – O/Mo	Percent (%)
W_0	*WO_3*	-	-	-	-	-
	MoO_2	-	1.837	3.836	2.088	39.46
	MoO_3	-	1	3.012	3.012	60.54
W_2	*WO_3*	7.114	-	21.106	2.967	2.69
	MoO_2	-	1.816	3.767	2.074	31.46
	MoO_3	-	1.00	3.010	3.010	61.85
W_4	*WO_3*	9.00	-	26.69	2.970	9.86
	MoO_2	-	1.837	3.765	2.049	52.12
	MoO_3	-	1.00	3.016	3.016	38.02

Table 3
Shows the crystallite size of W_0, W_2, and W_4 thin films.

Sample	FWHM(°)	2θ(°)	Crystallite Size(nm)
W_0	0.34422	23.25658	24.630
W_2	0.35396	23.31281	23.954
W_4	0.97084	23.35093	8.734

In comparison to the W_2 thin film, the MoO_2 phase grows as the number of W increases, whereas the MoO_3 phase decreases. Estimating crystallite size is calculated using the Scherrer equation (Ingham & Toney, 2013; Patterson, 1939; Zsigmondy & Scherrer, 1912) and shown in Table 3 for W_0, W_2, and W_4 thin films. The crystalline size of W_0 and W_2 thin films did not show a big difference. While for W_4, a sharp decrease in the crystalline size of 8.73nm was observed. XRD data showed that with the introduction of W into the structure, amorphization has also started in the film structure because the crystallization temperature of WO_3 is high.

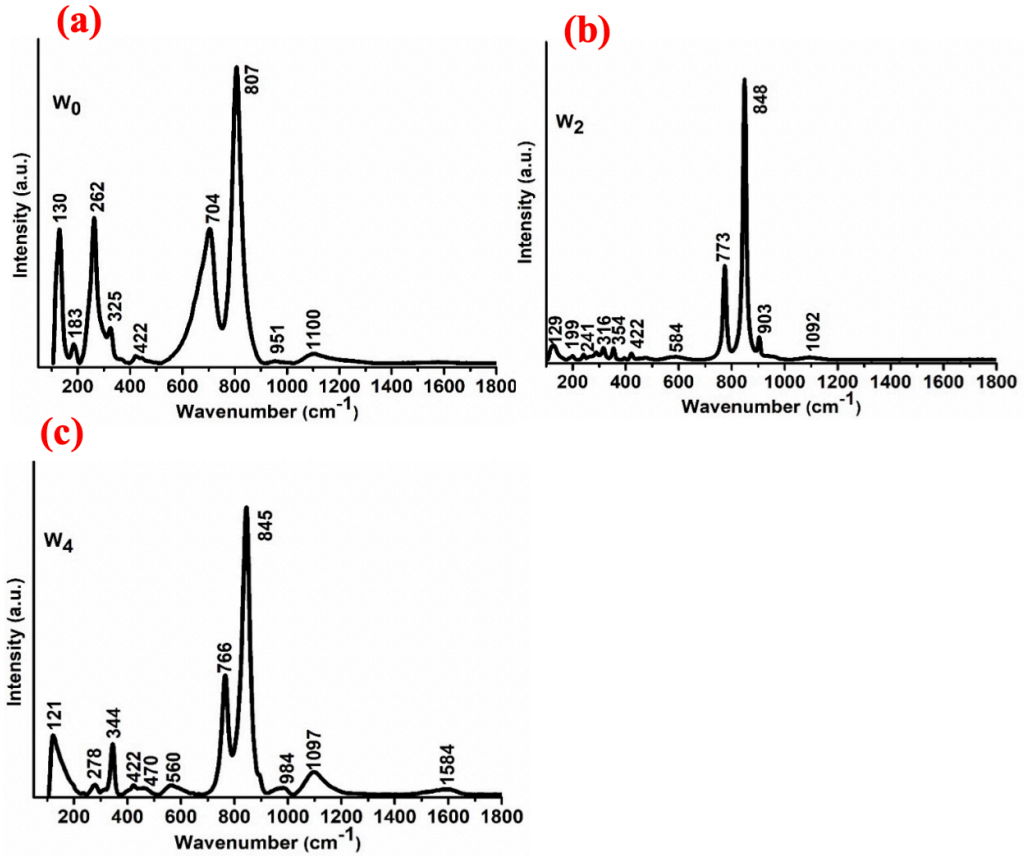

Figure 4. (a), (b), and (c) shows Raman spectra of W0, W2, and W4 doped Mo-O thin films, respectively.

The calculated crystallite sizes belong to the crystallized part of the structure and do not include the amorphous part. Raman spectra of W_0, W_2, and W_4 samples are shown in Fig. 4 (a), (b) and (c), respectively. The main Raman is attributed to peaks at 770 cm^{-1} to the stretching modes in the monoclinic WO_3 in W_2 and W_4 thin films (Gurlo et al., 2004; Y. S. Kim et al., 2008). The main Raman peaks at 807, 845, and 845 cm^{-1} are contributed to the stretching mode of the Mo-O bond.

3.2. Morphological and surface characterizations

SEM was used to characterize the morphology of the W_0, W_2, and W_4 samples, as shown in Fig. 5. An uneven nanosheet with significant particle size may be seen in the W_0 thin film. More regular structures emerged as the amount of W grew. While, for W_2 thin film, there was a mixture of nanosheets and nanorods, but for W_4 a shape like nanorods with a smooth surface and small crystallite size was observed. We thought also that the amount of W plays a meaningful role in the surface morphology of W_0, W_2, and W_4 thin films by controlling the amount of MoO_2. Elemental analyzes and distributions of W_0, W_2, and W_4 thin films grown on the Si substrate were performed using EDX spectroscopy as shown in Fig. 6. The quantitative elemental analysis was summarized in Table 4. As seen in EDX results, it was determined that W was homogeneously distributed in the Mo-O matrix. Fig. 7 shows the AFM images, where the surface roughness was decreased from W_0 to W_4. The high roughness and sharpness surface was owing to W_4 thin film which supports the high gas adsorption and optical sensing ability.

Table 4
Shows the quantitative analyses, weight, and atomic ratios in percentages for O (K series), W (L series), and Mo (L series) in W_0, W_2, and W_4 thin films.

Element		Thin Films		
		W_0	W_2	W_4
O (K series)	Weight%	75.97	76.68	77.14
	Atomic%	94.99	95.30	95.97
W (L series)	Weight%	0.00	1.38	7.23
	Atomic%	0.00	0.15	0.78
Mo (L series)	Weight%	24.03	21.95	15.64
	Atomic%	5.01	4.55	3.24

3.3. Optical properties

Optical properties calculations are important to study the film transmission (T) and absorbance (A) spectra. T and A spectra of the W_0, W_2, and W_4 thin films on a clean glass were conducted in the range of 300 to 1000 nm (Rodríguez-Carvajal, 1993). Fig. 8 (a) and (b) show the spectra of A and T, respectively. At 460 nm, a high transmission value of 97% was belonging to the W_4 thin film. In addition, W_0 and W_2 thin films show sharp edges of the basic absorption band close to λ = 400nm, while no peak was observed for the W_4 thin film. A slight blue shift in the optical absorption curve was observed by injecting W into the Mo-O_2 lattice which may relate to the electron transfer between Mo^{5+} and W^{6+} ions are being due to the electron gap transfer between Mo^{5+} and W^{6+} ions and to the quantum electron confinement in Mo. This result suggested that the absorption band in W_2 and W_4 thin film results from the discontinuous transfer of electrons (Hiruta et al., 1984; Schirmer et al., 1977).

The optical bandgap of the Mo-O compound can be changed by changing the W ratio, which affects photodetection and gas sensing ability (Taurino et al., 2003). To optical properties of these thin films, the optical bandgaps are calculated as below (Görmez et al., 2020). The optical absorption theory can be calculated from the equation with the association between the coefficient of absorption (α) and the photon energy (hν): $\alpha = \frac{B(h\nu - E_g)^x}{h\nu}$, where α can be calculated from the spectrum of transmission using $\alpha = \frac{1}{d} ln\left(\frac{1}{T}\right)$ and B, E_g, h and x are a constant, the optical bandgap, the Planck's constant and 0.5 for the directly allowed transitions while For indirect transitions, the x value is taken as 2, which also applies to the materials we investigate, respectively. The photon's energy is related to the direct bandgap E_g by the equation: $(\alpha h\nu)^2(h\nu - E_g)$. The E_g values were computed and plotted by extrapolating the linear component of $(\alpha h\nu)2$ vs. $h\nu$ at α=0. It is possible to obtain the E_g by extrapolating the linear component of the plot of $(\alpha h\nu)2$ vs. $h\nu$ to α=0. Fig. 9 (a), (b), and (c) display the computed band gaps of W0, W2 and W4 thin films. The bandgap of W0, W2 and W4 thin films was measured as 3.62, 3.31, and 3.97 eV, respectively.

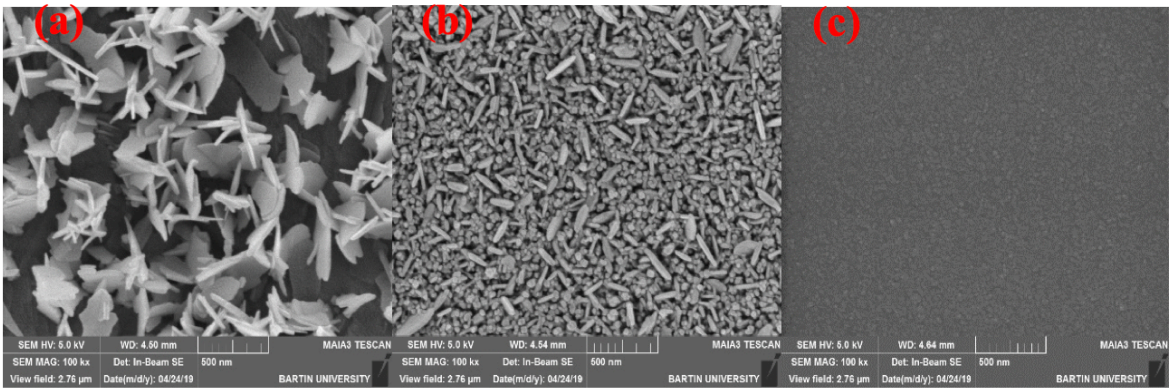

Figure 5. (a), (b), and (c) show SEM images of W_0, W_2, and W_4 doped Mo-O thin films, respectively.

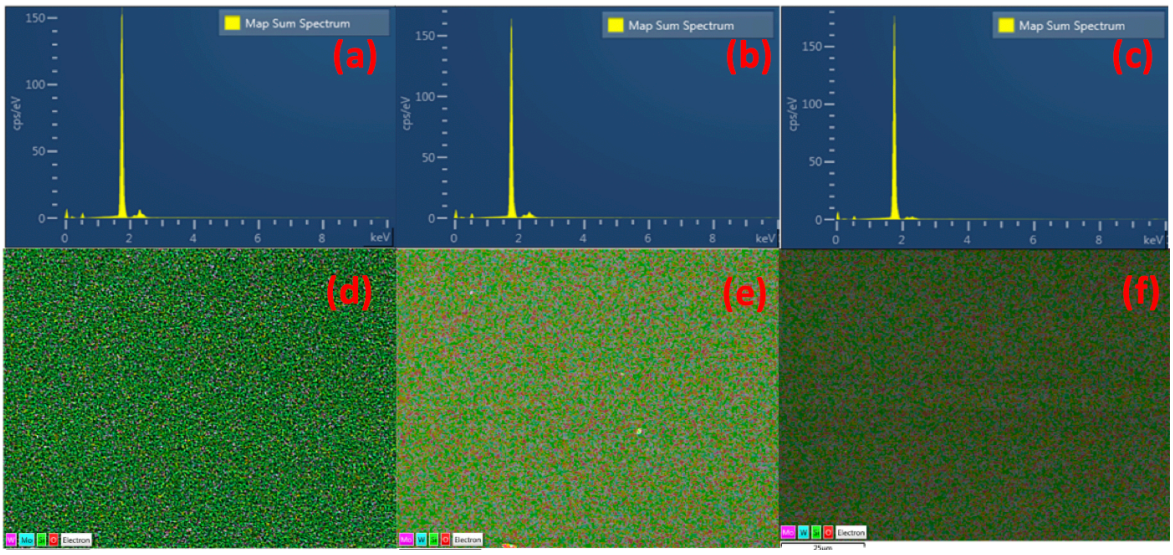

Figure 6. Shows the EDX spectra and the surface mapping of the as-prepared samples. Figures (a), (b), and (c) are representing the amount of Mo Lα1, O kα1, and W Lα1 on the Si substrate of W_0, W_2, and W_4 thin films, respectively. While, Figures (d), (e), and (f) are representing the surface mapping of W_0, W_2, and W_4 thin films, respectively. Where Si, O, W, and Mo are referring to green, red, aqua, and purple colors.

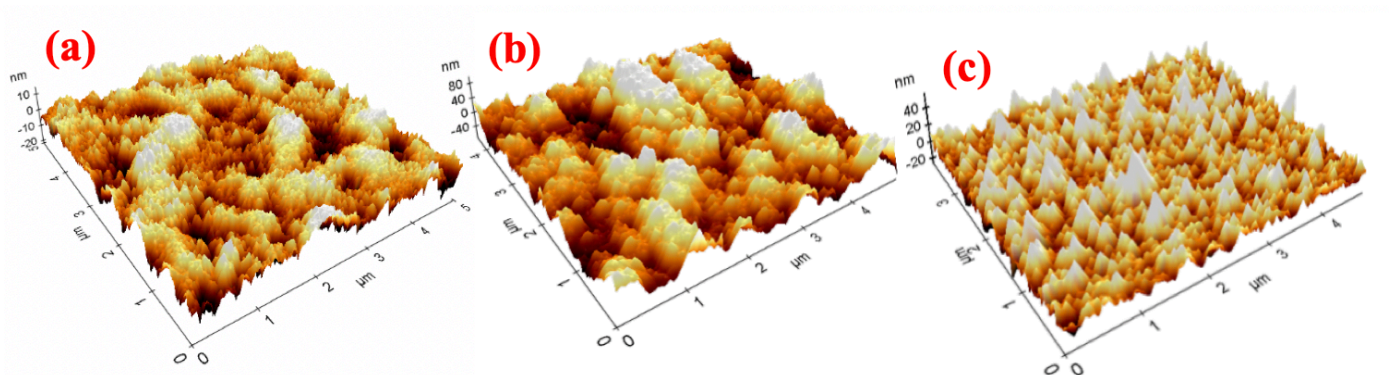

Figure 7. (a), (b), and (c) show AFM images of W_0, W_2, and W_4 doped Mo-O thin films, respectively.

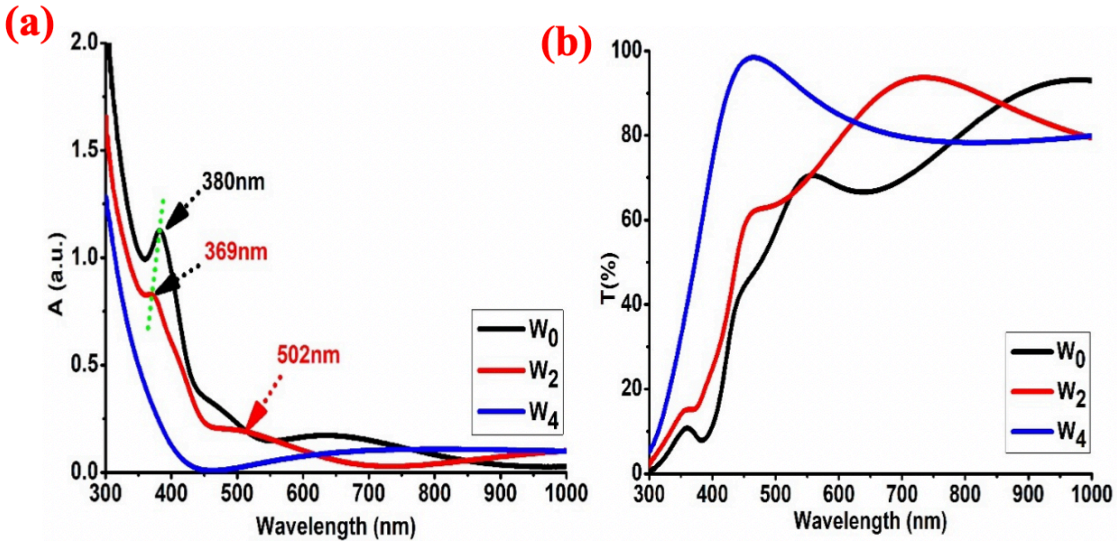

Figure 8. (a) and (b) show the transmission and absorption graphics of W_0, W_2, and W_4 doped Mo-O thin films, respectively.

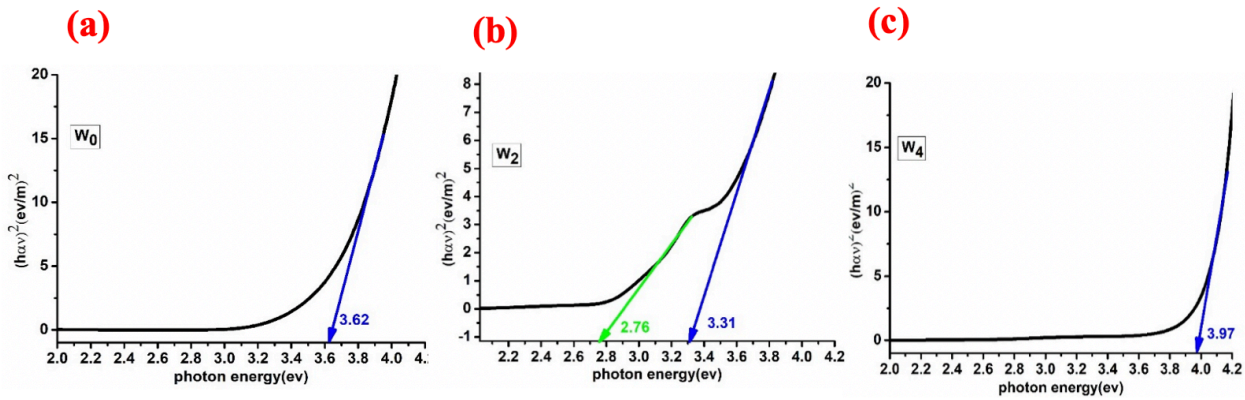

Figure 9. Shows the bandgap graphics of (a): W_0, (b): W_2 and (c): W_4 thin films. The intercept of the solid line with the horizontal axis can define the value of the bandgap.

3.4. Gas sensing measurements and parameters

3.4.1. Electrical, dynamical, and, sensitivity measurements

The forward voltage-current (V-I) in N_2 and CO_2 gas environments, respectively, is shown in Fig. 10 (a) and (b). Fig. 10 (c) and (d) exhibit the time-resistance (t-R) characterization of W_0, W_2, and W_4 thin films in CO_2 and N_2 gas, respectively. The Ohmic contacts on the W_0 and W_2 thin films are visible, whereas the Schottky contacts on the W_4 thin film are visible. Fig. 10 shows that the conductivity increased with increased W content. The total resistance of the films decreased with increasing W contents in the N_2 and CO_2 environment as seen in Fig. 10 (c) and (d). Due to the oxidation behavior of CO_2, the resistance of the sensors was decreased by introducing CO_2 which confirms its p-type conductivity as in Fig. 10 (d). To understand the sensor behavior of W_0, W_2, and W_4 thin films, the transient kinetics, sensitivity, and sensing period are calculated in detail and defined here.

The sensor dynamics were evaluated at different CO_2 concentrations from 5 to 30 sccm, as shown in Fig. 11 (a-c). The sensor resistance decreased by introducing CO_2 as a p-type behavior, while N_2 gas is re-stabilizing the sensor by increasing the resistance again as Fig. 11. The sensitivity of the sensor can be measured in percent as $S(\%) = \frac{R_{CO_2} - R_{N_2}}{R_{N_2}} * 100$, where R_{CO_2} and R_{N_2} are the sensor resistances of CO_2 and N_2, respectively. Fig. 11 (d) shows the sensitivity of W_0, W_2, and W_4 sensors with CO_2 concentration. It seems that the sensitivity of the W_4 sensor shows the highest value of 3.4% at 5sccm. While, at higher concentrations, the sensor shows a decrease in the recorded sensitivity, which makes this sensor works better at lower concentrations.

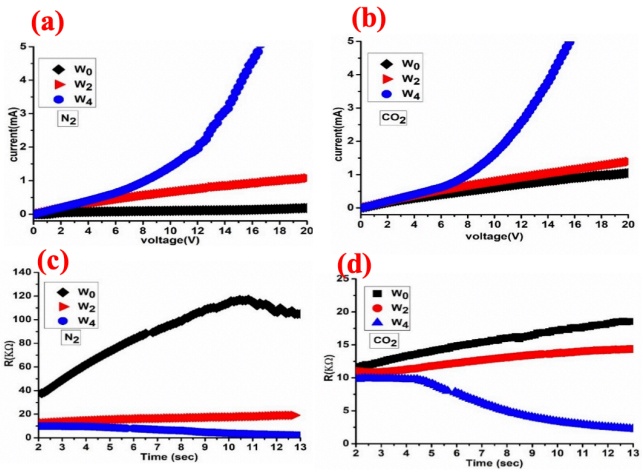

Figure 10. (a) and (b) show the current-voltage (I-V) graphics in the case of N_2 and CO_2 environments of W_0, W_2, and W_4, respectively. While (c) and (d) represent the change of resistance with time (R-t) in the case of N_2 and CO_2 environments of W_0, W_2, and W_4, respectively.

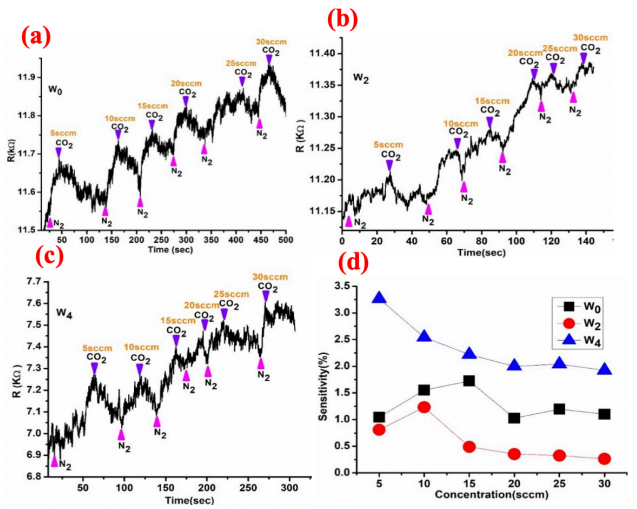

Figure 11. (a), (b), and (c) show the transit curves of W_0, W_2, and W_4 doped Mo-O thin films in a CO_2 environment, respectively. (d) shows the CO_2 gas sensitivity at different gas concentrations.

3.4.2. Response and recovery time

The forward voltage-current (V-I) in N_2 and CO_2 gas environments, respectively, is shown in Fig. 10 (a) and (b). Fig. 10 (c) and (d) exhibit the time-resistance (t-R) characterization of W_0, W_2, and W_4 thin films in CO_2 and N_2 gas, respectively. The Ohmic contacts on the W_0 and W_2 thin films are visible, whereas the Schottky contacts on the W_4 thin film are visible. The response time decreases with increasing W content as seen in Fig. 12 (a), with a very fast response time of less than 7 sec towards the W_4 sample. Similarly, the recovery time of W_4 thin film is reduced to 3sec at 30sccm.

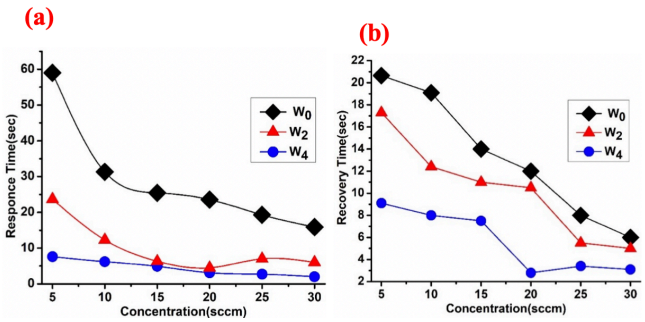

Figure 12. (a) and (b) show the response and recovery time of W0, W2, and W4 doped Mo-O thin films of CO2 at different gas concentrations, respectively.

3.5. UV-Photodetector measurements and parameters

3.5.1. Transient and optoelectronic response

Fig. 13 shows the optoelectronic applications of W_0, W_2, and W_4 thin films. Fig 13 (a-c) shows the dynamic behavior of W_0, W_2, and W_4 thin films under dark and 365nm UV illumination conditions, respectively. Each cycle has a switching time of 60sec and a bias voltage of 5V. The designed optical sensors were used to measure the time domain photoresponse in the case of ON/OFF and OFF/ON transitions of the UV light source, repeated many times for each 60sec at a bias voltage of 5V. A significant high photocurrent can be observed in the ON state at 5V, making the gate voltage lower the potential barriers at the contacts, resulting in highly efficient photogenerated carrier extraction and thus increasing the generated photocurrent. The gate voltage can affect the height of the Schottky barrier between the metal contact and film surface and thus shift the Fermi level (Das et al., 2013; Y. Yang et al., 2017). At a sweep voltage of +3 to -3V, the I-V curve has been plotted under dark and UV illumination for W_0, W_2, and W_4 thin films as Fig. 13 (d-f), respectively. All curves show a linear Ohmic contact through +3 to -3V. Fig. 13 (g-i) shows the log-current curves under dark and UV illumination of W_0, W_2, and W_4 thin films, respectively. It is seen that W doping may shift the logarithmic I-V curve towards the negative voltage region. Might fix this behavior due to the induced strain effects or unidirectional charge transport mechanism from the W to MoO_2-MoO_3 due to the different electron concentrations (Reddy et al., 2014). It is observed that under UV illumination a higher generated photocurrent value may be attributed to enhancement through the band-to-band excitation and the recombination of the carrier in the W-doped MoO_2-MoO_3 region. To test the long-term stability of all samples under both dark and UV illumination, a resistance-time (R-t) dynamic behavior over a long time was recorded and illustrated in Fig. 13 (j-n). All samples show symmetric kinetics through a 350sec period with remarkable differences in the generated photocurrent.

3.5.2. Photocurrent gain and photoresponsivity measurements

The induced photocurrent Iph is given by $I_{ph} = I_{Light} - I_{Dark}$, where I_{ph} can be modulated and increased according to the applied voltage and the power intensity (Ko et al., 2017). While Photocurrent gain (Pg) can be calculated as $P_g = (I_{photo} - I_{dark})/I_{dark}$, where I_{photo} and I_{dark} are current under light and dark conditions, respectively (Chao et al., 2016; Ko et al., 2017). While responsivity (R_λ) can be presented as $R_\lambda = \Delta I/(A \times P)$, where ΔI is the difference between the current in both light and dark conditions, A is the UV light illuminated area, and P is the light source power. Fig. 14 (a) shows the photocurrent and photocurrent gain of the W_0, W_2 and W_4 thin films sensors under 365nm UV illumination source. The generated photocurrent is directly proportional to the W contents and directly with the MoO_2 phase in W_2 and W_4 thin films. While W_2 thin film has the highest photocurrent gain of 0.13.

3.5.3. Responsivity, external quantum efficiency, and detective measurements

The responsivity of W_0, W_2, and W_4 thin films are in Fig. 14 (b). The responsivity of the W-doped MoO_2-MoO_3 UV detector shows high values ranging from 500 to 2500 A/W for W_0 and W_4 sensors. These values are higher than the 2.4 $mWcm^{-2}$ reported by X. Li *et al*, (Zhuo et al., 2018). The responsivity values show a linear increase with W content. It is known that more efficient light absorption can be involving more electron-hole (e-h) pair generation, resulting in higher mobility and more detection ability. External Quantum Efficiency (EQE) can be calculated as $EQE = \frac{hcR_\lambda}{e\lambda}$, where h is the Planck's constant (~ 4.135×10^{-15}eV.s), e is the charge of the electron (~1.602×10^{-9}C), c is the light velocity (~$3 \times 10^8 m/s^{-1}$), and λ is the shining wavelength (365 nm) (Wu & Chang, 2014). EQE can be used to generate the photocurrent I_{ph} and the fraction of the free carriers that are extracted to the photo-flux φ_{in} that can be collected at a given energy E_{ph}. The EQE values as a function of W_0, W_2, and W_4 thin films are plotted in Fig. 14 (b), where EQE varies from 1.3×10^9 to 5.5×10^9 at 365nm which is considered higher than the mesoscopic multilayer MoS_2 as reported before (Saenz et al., 2018). Another significant indicator of a

photodetector's value is the sensor's detectable signal (Ko et al., 2017), which can be referred to by the specific detectivity (in Jones), $D = \frac{(AB)^{0.5} R_\lambda}{i_n} \left(cmHz^{\frac{1}{2}} W^{-1} \right)$, where A is the sensor area of the d in cm², B is the bandwidth, and i_n is the observed noise current. If the shot noise from the dark current is the key source of noise, the particular detectivity can be simplified as $D = \frac{R_\lambda A^{0.5}}{(2eI_{dark})^{0.5}}$ (Liu et al., 2014). The calculated D* is depicted in Fig. 14 (c), where, the maximum D* is ~ 1.45× 10^8 Jones attributed for W_4 thin films and applied voltage of 5V.

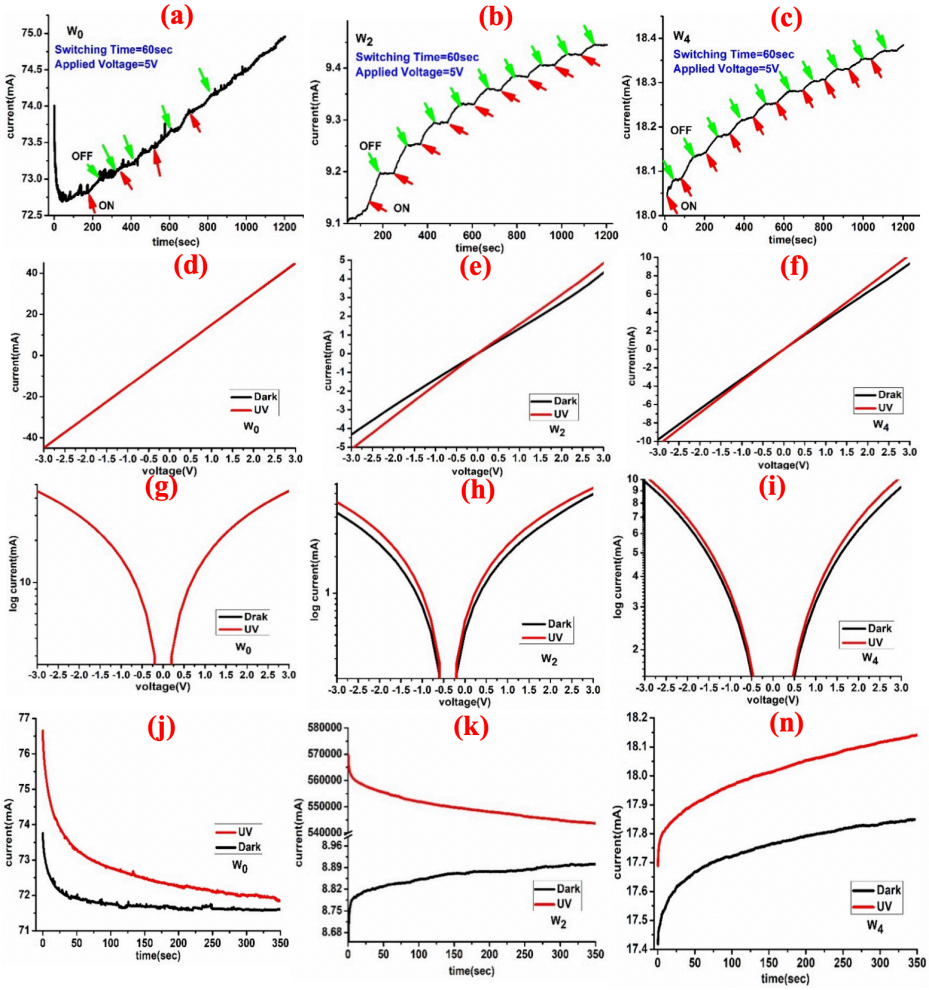

Figure 13. (a, b, and c), (d, e, and f), (g, h, and i), and (j, k, and n) show the optoelectronic characterizations of W_0, W_2, and W_4 doped Mo-O as an ON/OFF transit dynamic, linear current-voltage, semi-logarithmic scale current-voltage, and current-time steady-state curves in dark and under UV illumination, respectively.

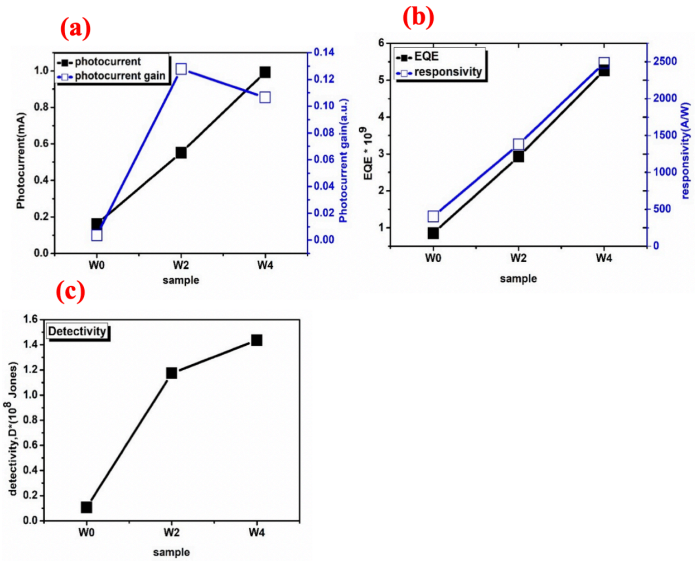

Figure 14. (a) Shows the photocurrent and photocurrent gain as a function of the sample. It is observing an increase in photocurrent with increasing the W amount in Mo-O with maximum value for W_2, while the photocurrent gain of W_4 shows the highest value. (b) Shows the change of EQE and responsivity as a function of W doped Mo-O samples. Increasing W content enhances the photoresponsivity and EQE values due to an increased photo-absorption observed. (c) Representing the Detectivity of the W-doped Mo-O photodetectors as a function of W contents in MoO_2-MoO_3 lattice.

4. Conclusion

The use of tungsten doping to modulate the surface of molybdenum oxide thin films has been reported. Using a reactive RF magnetron sputtering growth system with W and Mo targets, varied doping W contents into Mo may be prepared. The XRD Rietveld structure refinements have been carried out using the Fullproof Suite program to identify the crystallographic phases of the prepared samples. XRD analysis showed an increase in the MoO_2 content than MoO_3 in thin films by increasing the W doping. The films show a high transmission value. The W doping decreased the crystallite size from 24 nm to 8 nm which directly enhanced the UV photodetection and gas sensing ability at room temperature. The W doped MoO_2-MoO_3 thin films with a p-type gas sensing behavior towards CO_2 at room temperature. The film with high W content shows 3.5% gas sensing ability towards CO_2 at room temperature and a fast response and recovery time of less than 10sec at 5sccm CO_2. Meanwhile, the fabricated thin films show long-term stability as a UV photodetector. A high photocurrent and photocurrent gain of 1mA and 0.11 towards high W doping contents, respectively. The sensor was showing a high detectivity value of 1.41×10^8 Jones.

Acknowledgement

This work has been supported by the Scientific Research Projects Coordination Unit at Konya Necmettin Erbakan University with Grant No: 181710001.

References

Akdağ, A., Budak, H. F., Yilmaz, M., Efe, A., Büyükaydin, M., Can, M., Turgut, G., & Sönmez, E. (2016). Structural and Morphological Properties of Al doped ZnO Nanoparticles. *Journal of Physics: Conference Series*, *707*(1).

Bashiri, R., Samsudin, M. F. R., Mohamed, N. M., Suhaimi, N. A., Ling, L. Y., Sufian, S., & Kait, C. F. (2020). Influence of growth time on photoelectrical characteristics and photocatalytic hydrogen production of decorated Fe2O3 on TiO2 nanorod in photoelectrochemical cell. *Applied Surface Science*, *510*, 145482.

Basyooni, M. A., Eker, Y. R., & Yilmaz, M. (2020). Structural, optical, electrical and room temperature gas sensing characterizations of spin coated multilayer cobalt-doped tin oxide thin films. *Superlattices and Microstructures*, *140*, 106465.

Basyooni, M. A. M. A., Shaban, M., & El Sayed, A. M. A. M. (2017). Enhanced Gas Sensing Properties of Spin-coated Na-doped ZnO Nanostructured Films. *Scientific Reports*, *7*(1),

Basyooni, M. A., Zaki, S. E., Ertugrul, S., Yilmaz, M., & Eker, Y. R. (2020). Fast response of CO2 room temperature gas sensor based on Mixed-Valence Phases in Molybdenum and Tungsten Oxide nanostructured thin films. *Ceramics International*.

Boström, M., Gemmi, M., Schnelle, W., & Eriksson, L. (2004). Synthesis, properties and structure determination of Nb2O 3(SO4)2·1/4H2O from neutron and synchrotron X-ray powder diffraction data. *Journal of Solid State Chemistry*, *177*(4–5), 1738–1745.

Chao, C.-H., Weng, W.-J., & Wei, D.-H. (2016). Enhanced UV photodetector response and recovery times using a nonpolar ZnO sensing layer. *Journal of Vacuum Science & Technology A: Vacuum, Surfaces, and Films*, *34*(2), 02D106.

Çiftyürek, E., Sabolsky, K., & Sabolsky, E. M. (2016). Molybdenum and tungsten oxide based gas sensors for high temperature detection of environmentally hazardous sulfur species. *Sensors and Actuators, B: Chemical*, *237*, 262–274.

Çolak, H., & Karaköse, E. (2019). Synthesis and characterization of different dopant (Ge, Nd, W)-doped ZnO nanorods and their CO2 gas sensing applications. *Sensors and Actuators, B: Chemical*, *296*.

CRC Handbook of Chemistry and Physics. 81st Edition Edited by David R. Lide (National Institute of Standards and Technology). CRC Press: Boca Raton, FL. 2000. 2556 pp. $129.95. ISBN 0-8493-0481-4. (2000). *Journal of the American Chemical Society*, *122*(50), 12614–12614.

Das, S., Chen, H. Y., Penumatcha, A. V., & Appenzeller, J. (2013). High performance multilayer MoS2 transistors with scandium contacts. *Nano Letters*, *13*(1), 100–105.

Ghosh, A., Zhang, C., Shi, S., & Zhang, H. (2019). High temperature CO2 sensing and its cross-sensitivity towards H2 and CO gas using calcium doped ZnO thin film coated langasite SAW sensor. *Sensors and Actuators, B: Chemical*, *301*.

Görmez, A. E., Basyooni, M. A., Zaki, S. E., Eker, Y. R., Sönmez, E., & Yılmaz, M. (2020). Effect of in-/ex-situ annealing temperture on the optical, structural and gas sensing dynamics of CdS nanostructured thin films. *Superlattices and Microstructures*, *142*, 106536.

Gurlo, A., Bârsan, N., Oprea, A., Sahm, M., Sahm, T., Weimar, U., Kim, Y. S., Hwang, I. S., Kim, S. J., Lee, C. Y., & Lee, J. H. (2004). An n- to p-type conductivity transition induced by oxygen adsorption on α-Fe2O3. *Applied Physics Letters*, *85*(12), 2280–2282.

Haider, A. J., Shaker, S. S., & Mohammed, A. H. (2013). A study of morphological, optical and gas sensing properties for pure and Ag doped SnO2 prepared by pulsed laser deposition (PLD). *Energy Procedia*, *36*, 776–787.

He, S., Li, W., Feng, L., & Yang, W. (2019). Rational interaction between the aimed gas and oxide surfaces enabling high-performance sensor: The case of acidic α-MoO3 nanorods for selective detection of triethylamine. *Journal of Alloys and Compounds*, *783*, 574–582.

Hiruta, Y., Kitao, M., & Yamada, S. (1984). Absorption Bands of Electrochemically-Colored Films of WO3, MoO3and MocW1-cO3. *Japanese Journal of Applied Physics*, *23*(12), 1624–1627.

Hsu, K. C., Fang, T. H., Hsiao, Y. J., & Chan, C. A. (2020). Highly response CO2 gas sensor based on Au-La2O3 doped SnO2 nanofibers. *Materials Letters*, *261*.

Ingham, B., & Toney, M. F. (2013). X-ray diffraction for characterizing metallic films. In *Metallic Films for Electronic, Optical and Magnetic Applications: Structure, Processing and Properties* (pp. 3–38). Elsevier Ltd.

Jiang, W., Meng, L., Zhang, S., Chuai, X., Zhou, Z., Hu, C., Sun, P., Liu, F., Yan, X., & Lu, G. (2019). Design of highly sensitive and selective xylene gas sensor based on Ni-doped MoO3 nano-pompon. *Sensors and Actuators, B: Chemical*, *299*.

Juang, F. R., & Chen, B. Y. (2020). Effect of adding ZHS microcubes on ZnO nanorods for CO2 gas sensing applications. *Solid-State Electronics*, *164*.

Jung, G., Jeong, Y., Hong, Y., Wu, M., Hong, S., Shin, W., Park, J., Jang, D., & Lee, J. H. (2020). SO2 gas sensing characteristics of FET- and resistor-type gas sensors having WO3 as sensing material. *Solid-State Electronics*, *165*.

Kim, B. S., Kim, T. M., Choi, M. S., Shim, H. S., & Kim, J. J. (2015). Fully vacuum-processed perovskite solar cells with high

open circuit voltage using MoO3/NPB as hole extraction layers. *Organic Electronics*, *17*, 102–106.

Kim, Y. S., Hwang, I. S., Kim, S. J., Lee, C. Y., & Lee, J. H. (2008). CuO nanowire gas sensors for air quality control in automotive cabin. *Sensors and Actuators, B: Chemical*, *135*(1), 298–303.

Ko, P. J., Abderrahmane, A., Kim, N. H., & Sandhu, A. (2017). High-performance near-infrared photodetector based on nano-layered MoSe2. *Semiconductor Science and Technology*, *32*(6), 065015.

Lee, C. C., Biring, S., Ren, S. J., Li, Y. Z., Li, M. Z., Al Amin, N. R., & Liu, S. W. (2019). Reduction of dark current density in organic ultraviolet photodetector by utilizing an electron blocking layer of TAPC doped with MoO3. *Organic Electronics*, *65*, 150–155.

Li, Bin, Liu, J., Tian, S., Liu, B., Yang, X., Yu, Z., & Zhao, X. (2019). VO2-ZnO composite films with enhanced thermochromic properties for smart windows. *Ceramics International*.

Li, Bo, Song, H. Y., Deng, Z. P., Huo, L. H., & Gao, S. (2019). Novel sensitive amperometric hydrogen peroxide sensor using layered hierarchical porous A-MoO3 and GO modified glass carbon electrode. *Sensors and Actuators, B: Chemical*, *288*, 641–648.

Li, T., Zeng, W., Zhang, Y., & Hussain, S. (2015). Nanobelt-assembled nest-like MoO3 hierarchical structure: Hydrothermal synthesis and gas-sensing properties. *Materials Letters*, *160*, 476–479.

Li, Z., Wang, W., Zhao, Z., Liu, X., & Song, P. (2017). Facile synthesis and enhanced trimethylamine sensing performances of W-doped MoO 3 nanobelts. *Materials Science in Semiconductor Processing*, *66*, 33–38.

Liu, X., Gu, L., Zhang, Q., Wu, J., Long, Y., & Fan, Z. (2014). All-printable band-edge modulated ZnO nanowire photodetectors with ultra-high detectivity. *Nature Communications*, *5*.

Ma, Z. H., Yu, R. T., & Song, J. M. (2019). Facile synthesis of Pr-doped In2O3 nanoparticles and their high gas sensing performance for ethanol. *Sensors and Actuators, B: Chemical*.

Mane, A. A., & Moholkar, A. V. (2018). Palladium (Pd) sensitized molybdenum trioxide (MoO3) nanobelts for nitrogen dioxide (NO2) gas detection. *Solid-State Electronics*, *139*, 21–30.

Mo, Y., Tan, Z., Sun, L., Lu, Y., & Liu, X. (2020). Ethanol-sensing properties of α-MoO3 nanobelts synthesized by hydrothermal method. *Journal of Alloys and Compounds*, *812*.

Mohamed, M. M., Salama, T. M., Morsy, M., Shahba, R. M. A., & Mohamed, S. H. (2019). Facile strategy of synthesizing A-MoO3−x nanorods boosted as traced by 1% graphene oxide: Efficient visible light photocatalysis and gas sensing applications. *Sensors and Actuators, B: Chemical*, *299*.

Pal, S., Mukherjee, S., Nand, M., Srivastava, H., Mukherjee, C., Jha, S. N., & Ray, S. K. (2020). Si compatible MoO3/MoS2 core-shell quantum dots for wavelength tunable photodetection in wide visible range. *Applied Surface Science*, *502*.

Park, W. H., Lee, G. N., & Kim, J. (2018). Reactive-sputtered transparent MoO3 film for high-performing infrared Si photoelectric devices. *Sensors and Actuators, A: Physical*, *271*, 251–256.

Patterson, A. L. (1939). The scherrer formula for X-ray particle size determination. *Physical Review*, *56*(10), 978–982.

Reddy, M. S. P., Kim, B.-J., & Jang, J.-S. (2014). Dual detection of ultraviolet and visible lights using a DNA-CTMA/GaN photodiode with electrically different polarity. *Optics Express*, *22*(1), 908.

Rodríguez-Carvajal, J. (1993). Recent advances in magnetic structure determination by neutron powder diffraction. *Physica B: Physics of Condensed Matter*, *192*(1–2), 55–69.

Saenz, G. A., Karapetrov, G., Curtis, J., & Kaul, A. B. (2018). Ultra-high photoresponsivity in suspended metal-semiconductor-metal mesoscopic multilayer MoS 2 broadband detector from UV-to-IR with low schottky barrier contacts. *Scientific Reports*, *8*(1).

Schirmer, O. F., Wittwer, V., Baur, G., & Brandt, G. (1977). Dependence of WO3 Electrochromic Absorption on Crystallinity. *Journal of the Electrochemical Society*, *124*(5), 749–753.

Shaban, M., Attia, G. F., Basyooni, M. A., & Hamdy, H. (2014). Synthesis and characterization of Tin oxide thin film, effect of annealing on multilayer film. In L. Elnai & R. Mawad (Eds.), *J. Modern Trends in Phys. R* (Vol. 14).

Shaban, M., Attia, G. F., Basyooni, M. A., & Hamdy, H. (2015). Morphological and Structural Properties of spin coated Tin Oxide thin films. *International Journal of Engineering and Advanced Research Technology (IJEART)*, *1*(3), 11–14. www.ijeart.com

Shafieyan, A. R., Ranjbar, M., & Kameli, P. (2019). Localized surface plasmon resonance H2 detection by MoO3 colloidal nanoparticles fabricated by the flame synthesis method. *International Journal of Hydrogen Energy*, *44*(33), 18628–18638.

Sun, Q. J., Xu, Z., Zhao, S. L., Zhang, F. J., Gao, L. Y., & Wang, Y. S. (2010). The performance improvement in pentacene organic thin film transistors by inserting C60/MoO3 ultrathin layers. *Synthetic Metals*, *160*(21–22), 2239–2243.

Tanvir, N. Bin, Wilbertz, C., Steinhauer, S., Köck, A., Urban, G., & Yurchenko, O. (2015). Work Function Based CO2 Gas Sensing Using Metal Oxide Nanoparticles at Room Temperature. *Materials Today: Proceedings*.

Tanvir, N. B., Yurchenko, O., Laubender, E., & Urban, G. (2017). Investigation of low temperature effects on work function based CO2 gas sensing of nanoparticulate CuO films. *Sensors and Actuators, B: Chemical*, *247*, 968–974.

Taurino, A., Catalano, M., Rella, R., Siciliano, P., & Wlodarski, W. (2003). Structural and optical properties of molybdenum–tungsten mixed oxide thin films deposited by the sol-gel technique. *Journal of Applied Physics*, *93*(7), 3816–3822.

Touihri, S., Arfaoui, A., Tarchouna, Y., Labidi, A., Amlouk, M., & Bernede, J. C. (2017). Annealing effect on physical properties of evaporated molybdenum oxide thin films for ethanol sensing. *Applied Surface Science*, *394*, 414–424.

Wang, C., Liu, J., Yang, Q., Sun, P., Gao, Y., Liu, F., Zheng, J., & Lu, G. (2015). Ultrasensitive and low detection limit of acetone gas sensor based on W-doped NiO hierarchical nanostructure. *Sensors and Actuators, B: Chemical*, *220*, 59–67.

Wei, Q., Song, P., Li, Z., Yang, Z., & Wang, Q. (2019). Enhanced triethylamine sensing performance of MoO 3 nanobelts by RuO 2 nanoparticles decoration. *Vacuum*, *162*, 85–91.

Wei, Z., Hai, Z., Akbari, M. K., Qi, D., Xing, K., Zhao, Q., Verpoort, F., Hu, J., Hyde, L., & Zhuiykov, S. (2018). Atomic layer deposition-developed two-dimensional A-MoO3 windows excellent hydrogen peroxide electrochemical sensing capabilities. *Sensors and Actuators, B: Chemical*, *262*, 334–344.

Wu, J. M., & Chang, W. E. (2014). Ultrahigh responsivity and external quantum efficiency of an ultraviolet-light

photodetector based on a single VO2 microwire. *ACS Applied Materials and Interfaces*, *6*(16), 14286–14292.

Xu, J., Shen, Y., Wang, C., Dai, J., Tai, Y., Ye, Y., Shen, R., Wang, H., & Zachariah, M. R. (2019). Controlling the energetic characteristics of micro energy storage device by in situ deposition Al/MoO3 nanolaminates with varying internal structure. *Chemical Engineering Journal*, *373*, 345–354.

Yang, S., Lei, G., Lan, Z., Xie, W., Yang, B., Xu, H., Wang, Z., & Gu, H. (2019). Enhancement of the room-temperature hydrogen sensing performance of MoO 3 nanoribbons annealed in a reducing gas. *International Journal of Hydrogen Energy*, *44*(14), 7725–7733.

Yang, Y., Huo, N., & Li, J. (2017). Sensitized monolayer MoS2 phototransistors with ultrahigh responsivity. *Journal of Materials Chemistry C*, *5*(44), 11614–11619.

Yeh, T. H., Lee, C. C., Shih, C. J., Kumar, G., Biring, S., & Liu, S. W. (2018). Vacuum-deposited MoO3/Ag/WO3 multilayered electrode for highly efficient transparent and inverted organic light-emitting diodes. *Organic Electronics: Physics, Materials, Applications*, *59*, 266–271.

Yue, H. Y., Zhang, H. J., Huang, S., Lu, X. X., Gao, X., Song, S. S., Wang, Z., Wang, W. Q., & Guan, E. H. (2020). Highly sensitive and selective dopamine biosensor using Au nanoparticles-ZnO nanocone arrays/graphene foam electrode. *Materials Science and Engineering C*, *108*.

Zaki, S. E., Basyooni, M. A., Shaban, M., Rabia, M., Eker, Y. R., Attia, G. F., Yilmaz, M., & Ahmed, A. M. (2019). Role of oxygen vacancies in vanadium oxide and oxygen functional groups in graphene oxide for room temperature CO 2 gas sensors. *Sensors and Actuators, A: Physical*, *294*, 17–24.

Zeb, S., Peng, X., Yuan, G., Zhao, X., Qin, C., Sun, G., Nie, Y., Cui, Y., & Jiang, X. (2019). Controllable synthesis of ultrathin WO3 nanotubes and nanowires with excellent gas sensing performance. *Sensors and Actuators, B: Chemical*.

Zhao, C., Liang, Z., Su, M., Liu, P., Mai, W., & Xie, W. (2015). Self-Powered, High-Speed and Visible–Near Infrared Response of MoO_{3-x} /n-Si Heterojunction Photodetector with Enhanced Performance by Interfacial Engineering. *ACS Applied Materials & Interfaces*, *7*(46), 25981–25990.

Zheng, Q., Huang, J., Cao, S., & Gao, H. (2015). A flexible ultraviolet photodetector based on single crystalline MoO3 nanosheets. *Journal of Materials Chemistry C*, *3*(28), 7469–7475.

Zhuo, R., Wang, Y., Wu, D., Lou, Z., Shi, Z., Xu, T., Xu, J., Tian, Y., & Li, X. (2018). High-performance self-powered deep ultraviolet photodetector based on MoS2/GaN p-n heterojunction. *Journal of Materials Chemistry C*, *6*(2), 299–303.

Zsigmondy, R., & Scherrer, P. (1912). Bestimmung der inneren Struktur und der Größe von Kolloidteilchen mittels Röntgenstrahlen. In *Kolloidchemie Ein Lehrbuch* (pp. 387–409). Springer Berlin Heidelberg.